Tectonophysics 608 (2013) 1109–1121

Contents lists available at ScienceDirect

Tectonophysics

journal homepage: www.elsevier.com/locate/tecto

The February 6, 2013 M_w 8.0 Santa Cruz Islands earthquake and tsunami

Thorne Lay [a,*], Lingling Ye [a], Hiroo Kanamori [b], Yoshiki Yamazaki [c], Kwok Fai Cheung [c], Charles J. Ammon [d]

[a] *Department of Earth and Planetary Sciences, University of California Santa Cruz, Santa Cruz, CA 95064, USA*
[b] *Seismological Laboratory, California Institute of Technology, Pasadena, CA 91125, USA*
[c] *Department of Ocean and Resources Engineering, University of Hawai'i, Honolulu, HI 96822, USA*
[d] *Department of Geosciences, The Pennsylvania State University, University Park, PA, USA*

ARTICLE INFO

Article history:
Received 22 March 2013
Received in revised form 29 June 2013
Accepted 2 July 2013
Available online 12 July 2013

Keywords:
Great underthrusting earthquake
Vanuatu subduction zone
Tsunami on Santa Cruz Island
Shallow megathrust slip
Rupture modeling from seismic and tsunami waves
Southwest Pacific earthquake hazard

ABSTRACT

The Santa Cruz Islands region has high seismicity near a 90° bend in the boundary between the Pacific and Australian plates. Southward, along the Vanuatu island arc, the Australian plate under-thrusts the Pacific plate in a well-defined subduction zone. Westward, a transpressional, predominantly transform boundary extends to the southern Solomon Islands subduction zone. The Santa Cruz Islands region has upper plate strike-slip and normal faulting, plate boundary under-thrusting, outer rise extensional faulting, and intraplate compressional faulting. On February 6, 2013 the largest under-thrusting earthquake (M_w 8.0) that has been instrumentally recorded in the region ruptured the megathrust. The epicenter (10.738°S, 165.138°E) is about 1° north of epicenters of prior large shallow under-thrusting events in Vanuatu in 1934 (M ~ 7.8) and 1966 (M_S 7.9), and there is overlap of all three events' aftershock zones, but not their large-slip regions. At least 10 lives were lost, with 6 more missing, due to tsunami ~1.5 m high striking the town of Lata and several villages on the main Santa Cruz Island of Nendö (Ndeni) and a nearby small island Nibanga. Inundation of 500 m flooded the Lata airport. The tsunami was well-recorded by DART buoys spanning an unusually wide three-quadrant azimuthal aperture. Iterative modeling of teleseismic broadband P waves and the deep-water tsunami recordings resolves the slip distribution. There are two large-slip patches with a southeastward rupture expansion at about 1.5 km/s, with the second patch appearing to have ruptured with large slip at the trench. The event has relatively low short-period seismic wave energy release, but a typical overall moment-scaled total energy. The shallow rupture depth may be associated with the low level of short-period energy, and a near-total stress drop may account for a lack of underthrusting aftershocks among a highly productive aftershock sequence that included three events with $M_w \geq 7.0$.

1. Introduction

The boundary between the Pacific and Australian plates has strong contortions with complex faulting patterns near transitions between the Tonga, Vanuatu, and Solomon Islands arcs. These arcs have generally high levels of small and moderate size seismicity, and the largest events that have been instrumentally recorded have involved intraplate and interplate earthquakes with magnitudes up to about 8.0 (e.g., Allen et al., 2009; McCann et al., 1979; Nishenko, 1991), several of which were located near the abrupt bends in the arcs. Larger events in the future along the straight segments of the arcs cannot be ruled out, but in the seismological record there has been a tendency for spatial and temporal clustering of events with magnitudes of 7.0–8.0 in all three regions (e.g., Cleveland et al., 2013; Lay and Kanamori, 1980; Lay et al., 2010; Schwartz et al., 1989; Xu and Schwartz, 1993). In the northern Vanuatu arc there have also been several large event sequences in which the aftershock zone expanded markedly with time between 1 day and 1 year after the mainshock (e.g., Tajima and Kanamori, 1985a,b; Tajima et al., 1990). While it has been argued that these seismic manifestations simply fall within the expected range of behavior for all earthquake sequences (Felzer et al., 2004), the Solomon Islands and Vanuatu regions do appear to have particularly high earthquake productivity and greater than average numbers of earthquake doublets and triplets, suggesting that there are some regional attributes of the stress environment that favor unusually effective earthquake triggering interactions (e.g., Lay and Kanamori, 1980; Ruff, 1996).

On February 6, 2013, an M_w 8.0 earthquake (01:12:27 UTC, 10.738°S, 165.138°E, depth 28.7 km; http://comcat.cr.usgs.gov/earthquakes/eventpage/usc000f1s0#summary) struck near the Santa Cruz Islands along the northern end of the Vanuatu subduction zone (Fig. 1). The event has a shallow-dipping thrust faulting mechanism with the global Centroid-Moment Tensor (gCMT) solution (http://www.globalcmt.org/CMTsearch.html) best double-couple having strike 314°, dip 21°, and rake 74°, with a centroid depth of 27.6 km, and a centroid time shift of 28 s. Similar faulting geometries were

---

* Corresponding author. Tel.: +1 8314593164; fax: +1 8314593074.
E-mail address: tlay@ucsc.edu (T. Lay).

http://dx.doi.org/10.1016/j.tecto.2013.07.001

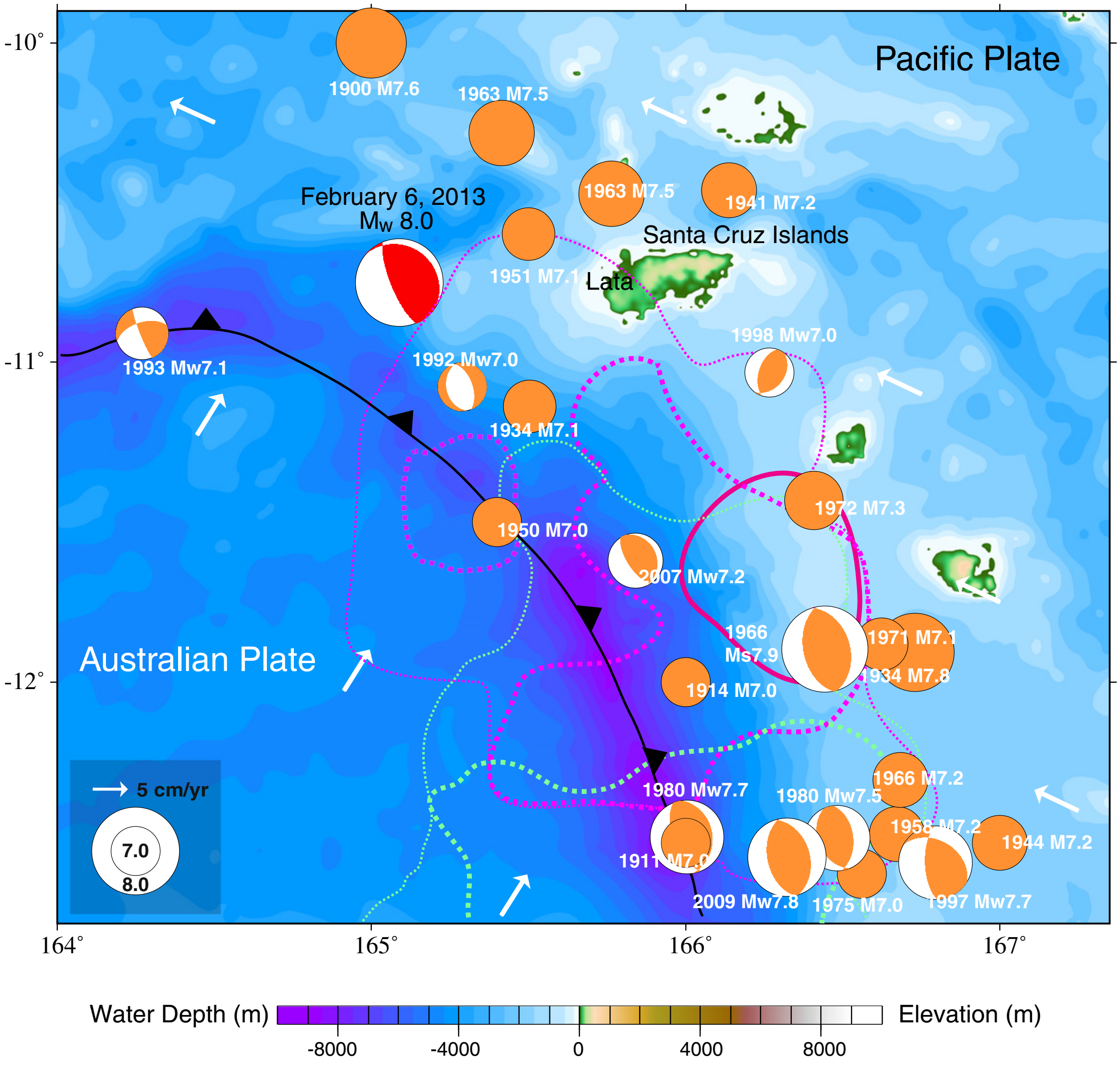

Fig. 1. Historical large earthquakes in the vicinity of the February 6, 2013, Santa Cruz Islands earthquake, with event locations and magnitudes taken from the PAGER catalog for the time interval 1900–1976 (orange dots, scaled proportional to estimated magnitudes, which are mostly from M_S) (Allen et al., 2009), and best-double-couple focal mechanism solutions from the global Centroid-Moment Tensor (gCMT) catalog, plotted at the USGS-NEIC epicentral locations, for events from 1976 to 2013 (orange faulting mechanisms, scaled proportional to M_w). The red focal mechanism for the 2013 event is the W-phase best-double-couple solution shown at the USGS epicenter. The white vectors indicate the relative plate motion velocities from the NUVEL-1 model. The focal mechanism shown for the 1966 M_S 7.9 earthquake is from Tajima et al. (1990). The solid magenta curve indicates the main slip zone estimated for the 1966 mainshock, with the 1-day and 10-day expanding aftershock zone extents being indicated by the large- and small-dash magenta outlines, respectively (Tajima and Kanamori, 1985a,b). Corresponding 1-day and 10-day expanding aftershock zone extents are indicated by the large- and small-dash green outlines, respectively for the July 17, 1980 (M_w 7.7) event.

reported by the USGS for long-period moment tensor inversions with source depths ranging from 15 to 32 km. The USGS estimated radiated seismic energy of 1.3×10^{15} J. The earthquake produced a tsunami of ~1.5 m height on the island Nendö (also called Santa Cruz Island or Ndeni) and a nearby small island, Nibanga, causing extensive coastal damage in the town of Lata and about 22 villages, including particularly hard-hit Nea and Velo. The tsunami inundated the Lata airport to ~500 m from the shoreline. There are 10 confirmed fatalities and 6 missing, with about 4000 homeless. Additional damage and one more fatality were caused by large aftershocks.

The 2013 Santa Cruz Islands earthquake is the largest regional event in the seismological record dating back to about 1900, with prior large events that were located north of the islands (Fig. 1) having magnitudes in the range 7.1–7.5 listed in the PAGER catalog (Allen et al., 2009). The locations of early events have substantial uncertainty, but none plot in the immediate vicinity of the 2013 epicenter and it is unclear whether any of the earlier events are on the megathrust. Toward the southeast from the epicenter there is a region of active interplate and intraplate faulting, with large events on July 18, 1934 [11.91°S, 166.73°E, M 7.8 (Pacheco and Sykes, 1992)] and December 31, 1966 [11.89°S, 166.44°E, M_S 7.9 (Tajima et al., 1990)], both of which had large aftershocks (July 21, 1934, M 7.1; December 31, 1966, M 7.2). There are no reports of large tsunami on the Santa Cruz Islands from these earlier events. Slightly further to the southeast, the Vanuatu subduction zone has had additional sequences of large events in 1980 and 2009, and a large intraplate event in 1997 (e.g., Cleveland et al., 2013; Kaverina et al., 1998). The 1966 and 1980 mainshocks produced aftershock sequences that expanded substantially between 1 and 100 days after the mainshocks (Tajima and Kanamori, 1985b), but it appears that their co-seismic large-slip regions did not overlap (Tajima et al., 1990). The 100-day aftershock zone for the 1966 event extends close to the 2013 epicenter, but the large-slip zone in 1966 is about 120 km southeast from the 2013 location (Fig. 1).

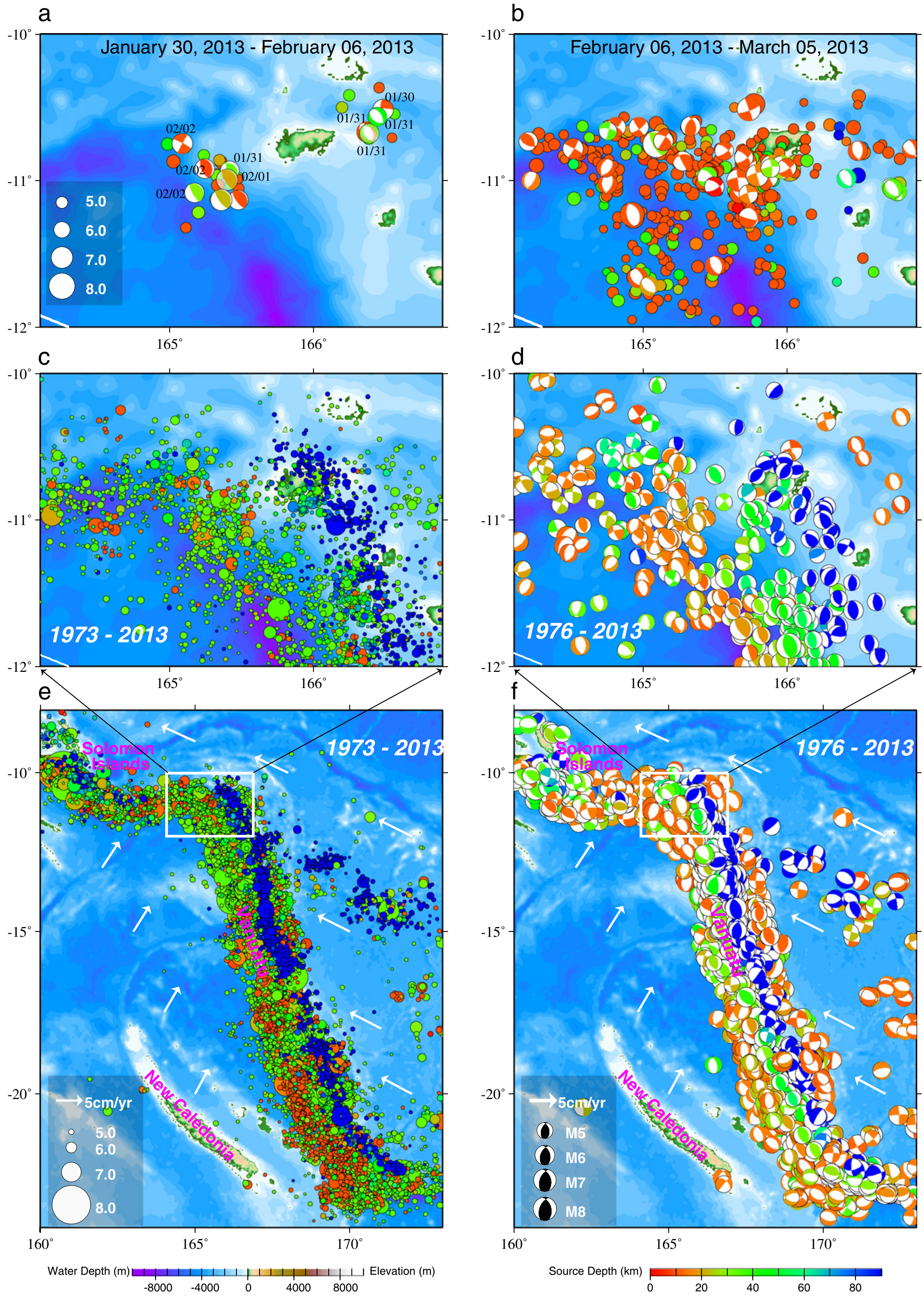

Fig. 2. The 2013 Santa Cruz Islands earthquake sequence with (a) the foreshock sequence beginning on January 30, 2013 and (b) the mainshock/aftershock sequence up to March 5, 2013 with available gCMT best-double-couple solutions shown at the USGS locations. The USGS earthquake catalog locations for magnitude 4.5–8.0 from 1973 to 2013, color-coded for source depth, is shown in (c) for the Santa Cruz Island region and (e) along the plate boundary from the southern Solomon Islands to southern Vanuatu. The gCMT focal mechanism catalog from 1976 to 2013 (best-double-couple solutions) plotted at the centroid locations for corresponding two areas are shown in (d) and (f).

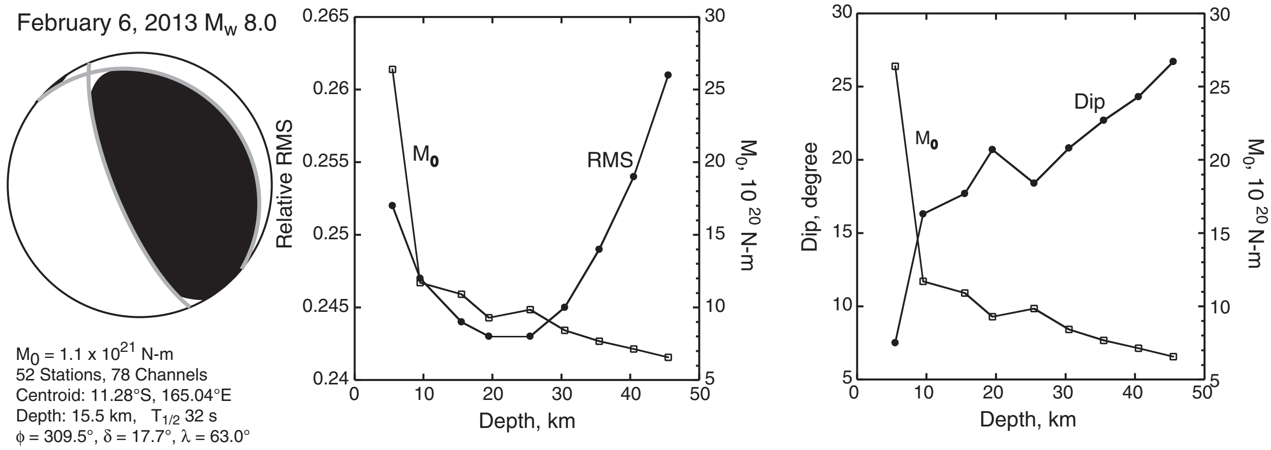

Fig. 3. Point-source moment tensor solution for the February 6, 2013 Santa Cruz Islands earthquake from inversion of W-phase observations in the frequency band 0.00167–0.005 Hz. The number of stations and channels used in the inversion is indicated, with representative comparisons of data and synthetics shown in Fig. 4. The seismic moment (M_0), centroid epicenter and depth, centroid time shift ($T_{1/2}$) and strike (ϕ), dip (δ) and rake (λ) of the best double couple solution are shown on the left. The trade-off curves or inversion relative RMS residual waveform misfit, M_0 and dip are shown for inversions with centroid depths ranging from 5.5 to 45.5 km.

The 2013 Santa Cruz Islands event was preceded by several upper plate strike-slip and normal faulting events with M_w 5.8 to 6.1 on January 30, 2013, followed by 5 interplate thrust faulting events with M_w 5.5 to 6.4 from January 31 to February 2. Then strike-slip faulting occurred from February 2 to 6 with M_w 5.9 to 6.0 (Fig. 2(a)). This diversity of faulting activity in the foreshock sequence persisted after the mainshock, with widespread aftershock activity involving a wide-range of faulting geometries, albeit with a notable lack of interplate thrust faulting (Fig. 2(b)). The prior seismicity distribution and accumulated focal mechanisms in the Santa Cruz Islands region and along the contorted plate boundary from the Solomon Islands to Vanuatu (Fig. 2(c–f)) indicate that most areas of intraplate and interplate seismicity in the 2013 sequence had limited preceding seismicity for several decades, notably the region trenchward of the Santa Cruz Islands. Combined with the lack of prior large earthquakes in the vicinity of the mainshock dating back over a century (Fig. 1), this suggests distinct earthquake behavior relative to the very active region of the Vanuatu subduction zone to the southeast, where large earthquake ruptures have struck every few decades during the seismological record.

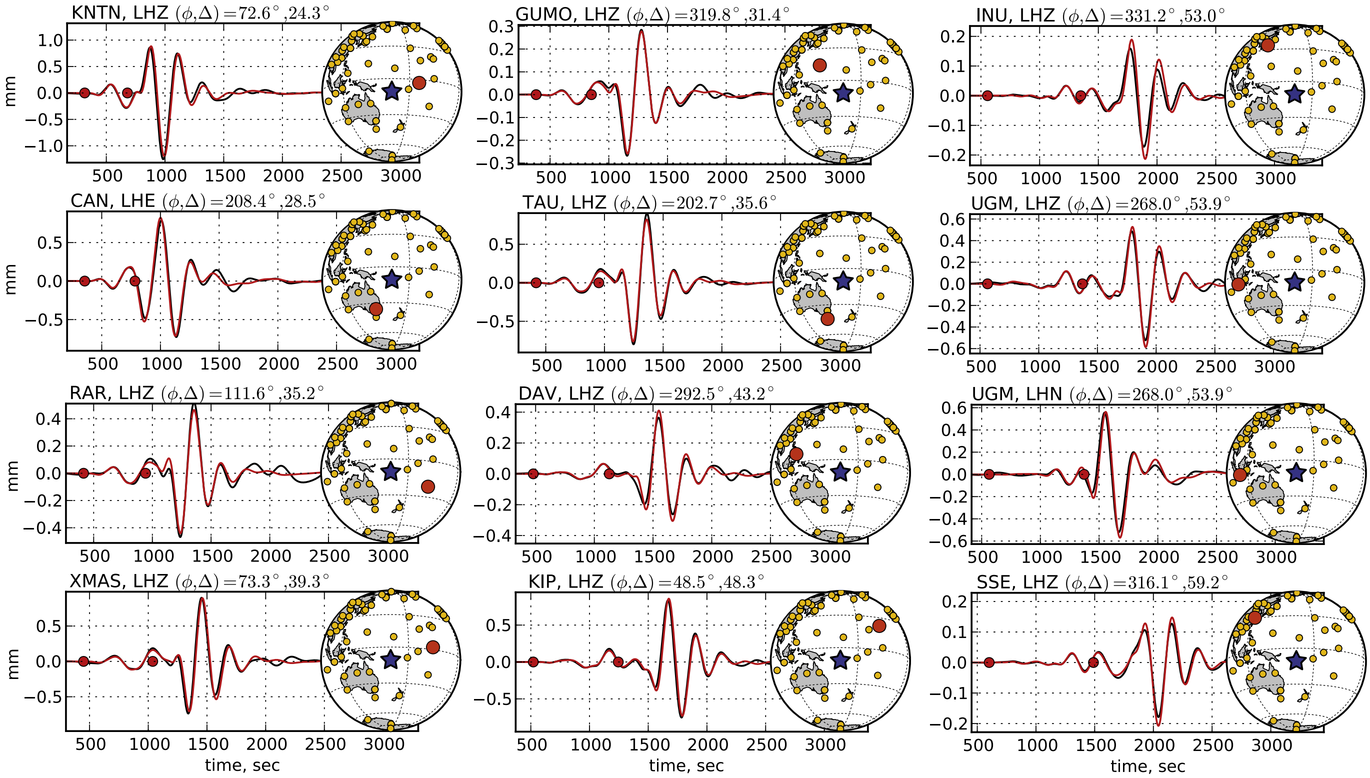

Fig. 4. Example W-phase observations (black traces) and computed waveforms (red) for the point-source moment tensor in Fig. 3 for the February 6, 2013 Santa Cruz Islands event. The data are from global seismic network stations with ground displacement filtered in the frequency band 0.00167–0.005 Hz. The W-phase signal used in the inversions is the waveform interval between the red dots. The large amplitude signals after the W-phase are fundamental mode surface waves and the waveform comparisons are predictions for those signals. The maps indicate the position of the station (red dot) among the total set of stations (gold dots) used in the corresponding W-phase inversion. Comparable waveform matches are found for all of the stations indicated in the maps.

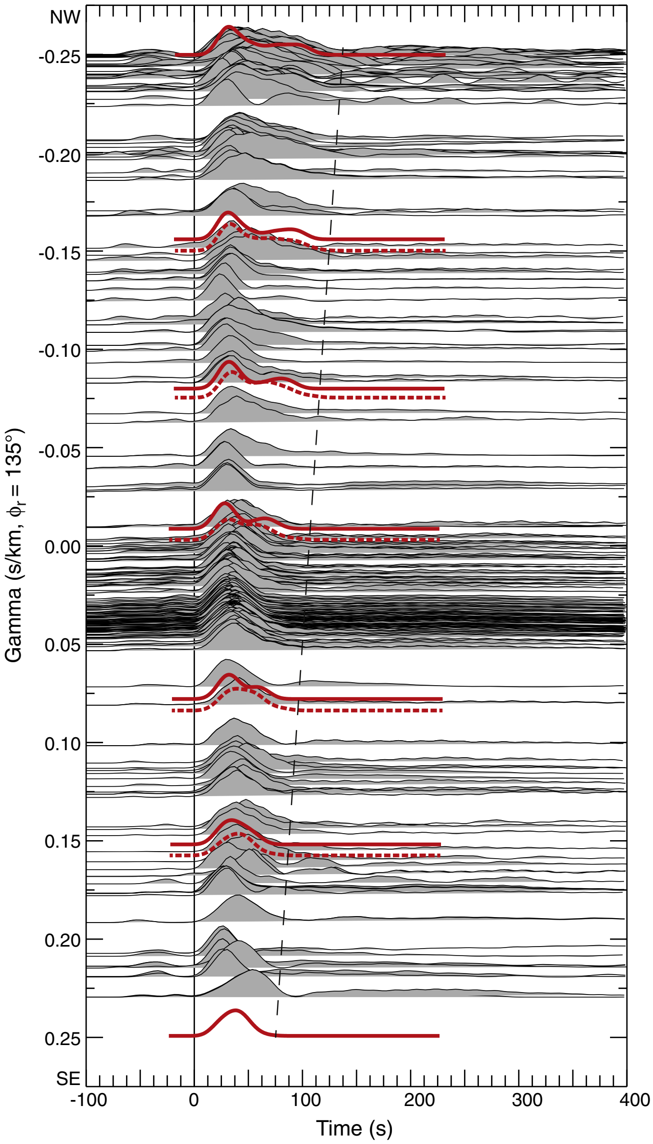

Fig. 5. Effective source time functions for R1 Rayleigh waves for the February 6, 2013 Santa Cruz Islands earthquake, plotted as a function of directivity parameter, gamma, for a rupture azimuth of 135°, assuming a phase velocity of 4.0 km/s. Each source time function is obtained by deconvolving the group-velocity windowed Rayleigh wave arrival by a point-source synthetic made by normal mode summation using the W-phase moment tensor source. This removes most propagation effects and allows azimuthal patterns in the source functions to be analyzed for rupture directivity. The red solid and dotted lines are predicted R1 source functions at corresponding values of directivity parameter for the finite-fault model shown in Fig. 6. The source functions narrow toward the SE due to a component of unilateral direction toward the azimuth in the rupture process.

Seismic and tsunami observations are modeled here to constrain the rupture process and slip distribution of the 2013 Santa Cruz Islands mainshock. In combination with consideration of the complex aftershock sequence, we characterize the overall significance of this great earthquake in the regional tectonic setting.

2. Mainshock rupture process characterization

Globally recorded digital seismograms for the February 6, 2013 Santa Cruz Islands earthquake from the Incorporated Research Institutions for Seismology (IRIS) Global Seismic Network and other Federation of Digital Seismic Networks (FDSN) were obtained from the IRIS Data Management Center and analyzed in conjunction with tsunami recordings to determine a model for the mainshock rupture. Three-component W-phase signals in the 0.00167–0.005 Hz passband were inverted for point-source moment tensors for a range of source depths using the procedure of Kanamori and Rivera (2008). Fig. 3 displays the moment tensor solution for a centroid depth of 15.5 km, along with the variations of inversion RMS residual, seismic moment, and dip with assumed source depth. The inversions provide the best waveform fits for source depths from 15.5 to 25.5 km, with examples shown in Fig. 4 for a depth of 15.5 km. For source depths shallower than 10 km the fit to W-phase waveforms degrades, along with overestimation of the long-period fundamental mode surface waves that arrive immediately afterward. Those surface waves are well predicted for a 15.5 km source (Fig. 3). Source depths greater than 30 km also degrade the fit to the W-phase waveforms and underpredict the long-period surface wave signals. The best double-couple solution for a 15.5 km source depth has strike 309.5°, dip 17.7° and rake 63°. This thrust-faulting mechanism is similar to the gCMT solution obtained for a larger centroid depth. The centroid time for this preferred W-phase solution is 32 s and the seismic moment is 1.1×10^{21} Nm (M_w 8.0).

We evaluated first-order characteristics of the rupture finiteness using Rayleigh wave directivity and back-projections of short-period network data. For the surface wave analysis we deconvolved observed group-velocity-windowed R1 Rayleigh wave signals from global FDSN stations by point-source normal-mode synthetic seismograms computed using the gCMT moment tensor for the PREM Earth model following the method described by Ammon et al. (2008) and Lay et al. (2009). The resulting propagation-corrected relative source time functions (STFs) show azimuthal variations in total duration and signal shape that can be used to estimate rupture attributes. By searching over all possible unilateral rupture directions, aligning the R1 STFs according to associated directivity parameters, the most systematic pattern to be detected was for a rupture azimuth of 135°, which is close to the local trench orientation (Fig. 1) and the negative strike direction of the shallow northeastward-dipping thrust plane of the W-phase solution (Fig. 3). The corresponding profile of STFs ordered by directivity parameter assuming a reference phase velocity $c = 4$ km/s (appropriate for the 80 s period R1 waves for model PREM) is shown in Fig. 5. The STFs are aligned on the source function onsets, with a dashed line indicating the approximately linear trend of total STF durations which range from $T_{max} = 137$ s to $T_{min} = 75$ s. For a simple unilateral rupture model approximation, the range in STF duration suggests a rupture length $L = c / 2 \times (T_{max} - T_{min}) = 124$ km. If we assume that the rise time, τ, is about 20% of the average duration, $T_{avg} = 106$ s, an approximate unilateral rupture velocity, $V_r = L / (T_{avg} - \tau) = 1.5$ km/s is obtained for a rupture azimuth of 135°. These values are not tightly resolved and the STFs show waveform variations that suggest the slip is not uniform during the rupture, but the STF analysis does provide some overall source characteristics that we use to constrain finite-fault modeling below.

To provide additional constraint on the finite-source modeling, we examined back-projections of short-period (1.0–4.0 s) P wave signals posted on the IRIS website for this event (http://www.iris.edu/spud/backprojection). Three networks of stations in North America, Europe and Australia were used for back-projections, with procedures described by Xu et al. (2009) and Trabant et al. (2012). While there are differences in the back-projections for the different networks, all of the images indicate a component of southeastward rupture expansion for the short-period radiation, with a secondary burst of energy 60 s into the rupture located about 80–100 km from the hypocenter. This indicates a rupture velocity of about 1.3–1.7 km/s, compatible with the value found from the R1 STF directivity. The short-period radiation images are not uniform with time and suggest two main intervals of radiation.

Guided by the W-phase best double couple solution and the STF and back-projection observations, we developed a finite-fault rupture

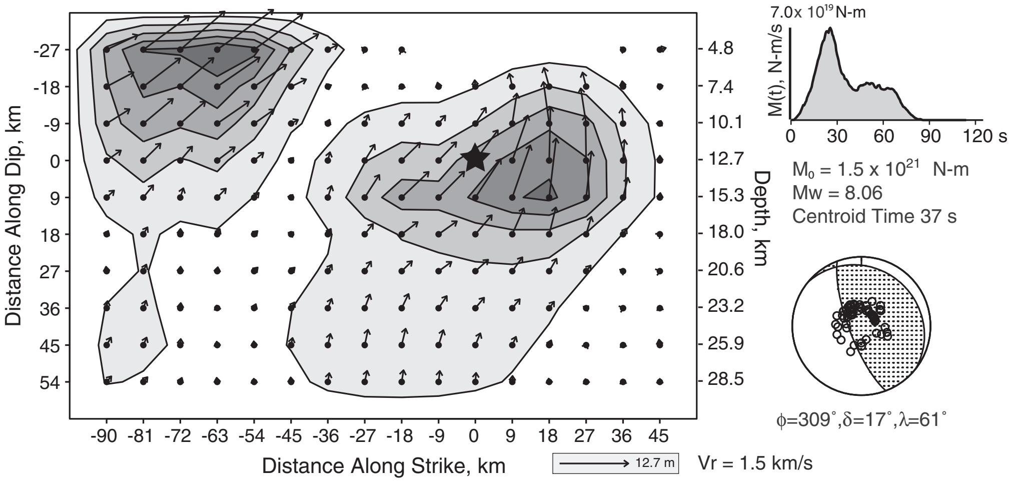

Fig. 6. Finite-fault slip model from teleseismic body wave inversion for the February 6, 2013 Santa Cruz Islands earthquake. The slip distribution on the fault plane is shown with the arrows indicating average rake of each subfault and slip magnitude being contoured (contour increment is 2.8 m). The hypocenter is indicated by the star. Peak slip is indicated, along with the rupture expansion velocity, Vr. The moment rate function, seismic moment, M_w, centroid time, and average focal mechanism are shown, with the lower hemisphere equal area projections indicating the positions sampled by teleseismic P waves used in the inversion. Tsunami observations were used to constrain the solution by iterative modeling. Observed and synthetic P wave comparisons are shown in Fig. 7.

model for the 2013 Santa Cruz Islands event by inverting teleseismic broadband P waves with ground motions in the period range 1–200 s using linear inversions with constant rupture velocity as in the approach of Kikuchi and Kanamori (1991). The rupture model was specified to have 10 rows of 9 km × 9 km subfaults along dip and 16 columns along strike. The subfault source time functions were parameterized by 7 symmetric 2-s rise time triangles, shifted by 2-s each, allowing total subfault durations of up to 16 s. Rake was allowed to vary for each subevent of each subfault to keep the problem linear. Modest smoothing was applied to stabilize the temporal and spatial moment distribution. The fault orientation has dip 17° and strike 309°, with asymmetry of the fault extent toward the southeast being allowed after initial inversions confirmed that was a preferred direction for overall rupture expansion. A source region crustal velocity model based on Crust2.0 (Bassin et al., 2000) was used. Initial inversions assumed the hypocentral parameters given by the USGS parameters, and satisfactory fits to the teleseismic P waves were obtained with spatially concentrated slip distribution similar to that of the on-line USGS finite-fault solution. However, comparisons with tsunami observations as discussed below indicated that models with the centroid of slip being deeper than 15 km under-predicted several tsunami recordings, and the most satisfactory models for both seismic wave and tsunami observations were found by moving the hypocenter shallower, to a depth of 12.7 km about 9 km up-dip from the USGS hypocenter and 18 km toward the southeast. A rupture velocity of 1.5 km/s was used for the preferred model shown in Fig. 6. The teleseismic P wave data do not tightly resolve this value, so we relied on the R1 STF and back-projection analysis to specify this choice. Comparisons of about half of the observed and modeled P wave signals are shown in Fig. 7.

Two large-slip regions were consistently found in inversions for fault models extending to the trench with hypocenters from 10 to 20 km. The two slip patches for the model in Fig. 6 are separated by about 90 km, compatible with the two bursts seen in the short-period P wave back-projections, with 60 s time separation. The moment rate function has two corresponding pulses, each about 30 s in duration, with the first one having about twice the moment of the second one. The overall centroid time shift is about 37 s, with a seismic moment of 1.5×10^{21} N-m (M_w 8.1). These values are basically compatible with the W-phase solution in Fig. 3, allowing for an increase in estimated seismic moment due to the modest decrease in source depth. The second slip-pulse is at very shallow depth, near the trench, and even though the moment is lower, the slip is larger than for the slip patch near the hypocenter due to a decrease of rigidity in the shallow crustal layers in the model. The overall shape of the moment rate function and the source directivity are compatible with the R1 STFs: predictions of the STFs for different directivity parameters are compared with the observations in Fig. 5. The P waveforms also indicate the dominance of the first subevent (Fig. 7). The back-projection data suggest that the second subevent radiated relatively little coherent short-period seismic wave energy in the southeastern region compared to the region around the hypocenter. This may be associated with rupture of the near-trench megathrust, which may have a higher proportion of sediments with distinct frictional properties.

3. Modeling of rupture and tsunami processes

The preferred finite-fault rupture model was obtained by iterative inversion of P-wave signals and forward modeling of tsunami observations; the latter was particularly valuable for constraining the depth extent of the rupture (Lay et al., 2011; Yamazaki et al., 2011b). NOAA deep-water bottom pressure sensors, known as DART, recorded clear signals of the tsunami with unusually good azimuthal distribution spanning three quadrants rather than the less than two quadrants typically spanned for circum-Pacific thrust events. The recorded tsunami data are sensitive to subtleties of the source mechanism and slip distribution as long as the complex propagation effects are reliably accounted for. We iteratively adjusted the hypocentral parameters and depth extent of the finite-fault model grid to reproduce the DART observations through modeling of nonlinear and dispersive ocean wave processes. Tide gauges in Hawaii also recorded signals of the tsunami, but their modulation by resonance modes of the insular shelves obfuscates direct inference of the source characteristics (Munger and Cheung, 2008). The tide gauge data, which are not considered in the iterative procedure, still allow independent validation of the final model.

The shock-capturing dispersive wave model NEOWAVE of Yamazaki et al. (2009, 2011a,b) describes the tsunami from its generation by an earthquake rupture model to propagation across the ocean reaching the water-level stations. For a specific finite-fault inversion of the teleseismic P waves, the planar fault model of Okada (1985) defines the kinematic seafloor deformation with time-varying subfault contributions and provides the seafloor vertical and horizontal displacement and velocity as input to NEOWAVE. The staggered finite difference model builds on the nonlinear shallow-water equations with a vertical velocity term to account for weakly-dispersive waves and a momentum

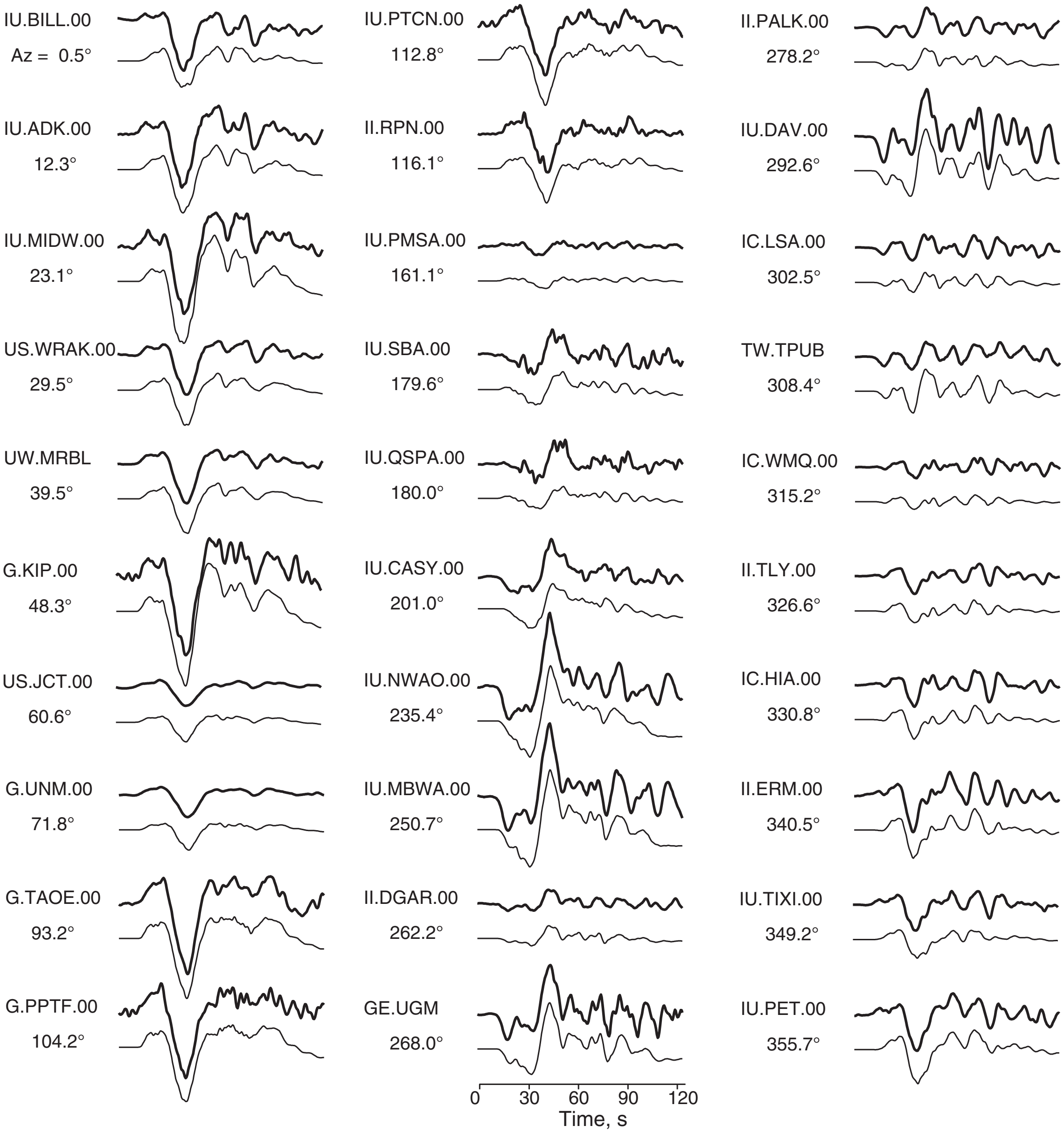

Fig. 7. Comparison of observed (bold lines) and modeled (thin lines) teleseismic P waves for the February 6, 2013 Santa Cruz Islands earthquake. The model shown in Fig. 6 is used for the computations. The signals are broadband ground displacements in the passband 0.005–0.9 Hz. Comparable waveform matches are found for all 61 stations used in the inversion.

conservation scheme to describe bores or hydraulic jumps. The vertical velocity term also accounts for the time sequence of seafloor uplift and subsidence, while the method of Tanioka and Satake (1996) approximates the vertical motions resulting from the seafloor horizontal deformation on the slope of the upper plate near the trench. We utilize a 1-arcmin (~1800 m) grid to model the near-field tsunami around the Santa Cruz Islands. Modeling of the far-field tsunami requires up to four levels of two-way nested grids with 2 arcmin (~3600 m) grid for propagation in the western Pacific, 24 arcsec (~720 m) grid for wave transformation across the Hawaiian islands, and 3 arcsec (~90 m) grid around the island coasts for transition to 0.3 arcsec (~9 m) grid at the tide gauges. The digital elevation model consists of the 1-arcmin ETOPO1 bathymetry for the western Pacific and multibeam and LiDAR data of finer than 50 and 3 m resolution around the Hawaiian Islands.

Fig. 8 shows map views of the slip model with bathymetry, seafloor displacement, and maximum tsunami amplitude for the final finite-source model in Fig. 6. The slip distribution produces two distinct uplift patches near Nendö (Santa Cruz Island) and along the trench that define the tsunami characteristics across the Pacific. While the sea surface elevation and seafloor uplift of 2.8 and 3.3 m at the northwest slip patch are similar, the surface elevation of 1.5 m at the southeast slip patch is significantly smaller than the uplift of 2.4 m due to wave dispersion over the narrow large slip region and increase in water depth. Fig. 9 illustrates the generation and near-field transformation of the tsunami (see supplemental material Animation S1). The rupture that begins at the northwest slip patch generates a distinctive initial wave to the west of Nendö in 37 s. A second wave from the southeast slip patch becomes fully developed 35 s later. The two initial pulses develop into well-defined radial waves within 3 min of the earthquake. The wave from the larger northwest slip patch dominates the tsunami. The slightly elongated slip patches along the trench result in primary energy propagation in the southwest and northeast directions. The snapshots at 6 and 9 min show constructive interference, shoaling, and refraction of the two radial waves over the insular shelf near western Nendö. The waves reach 1.8 m amplitude over the insular shelf and up to 3.4 m surface elevation locally corroborating reported

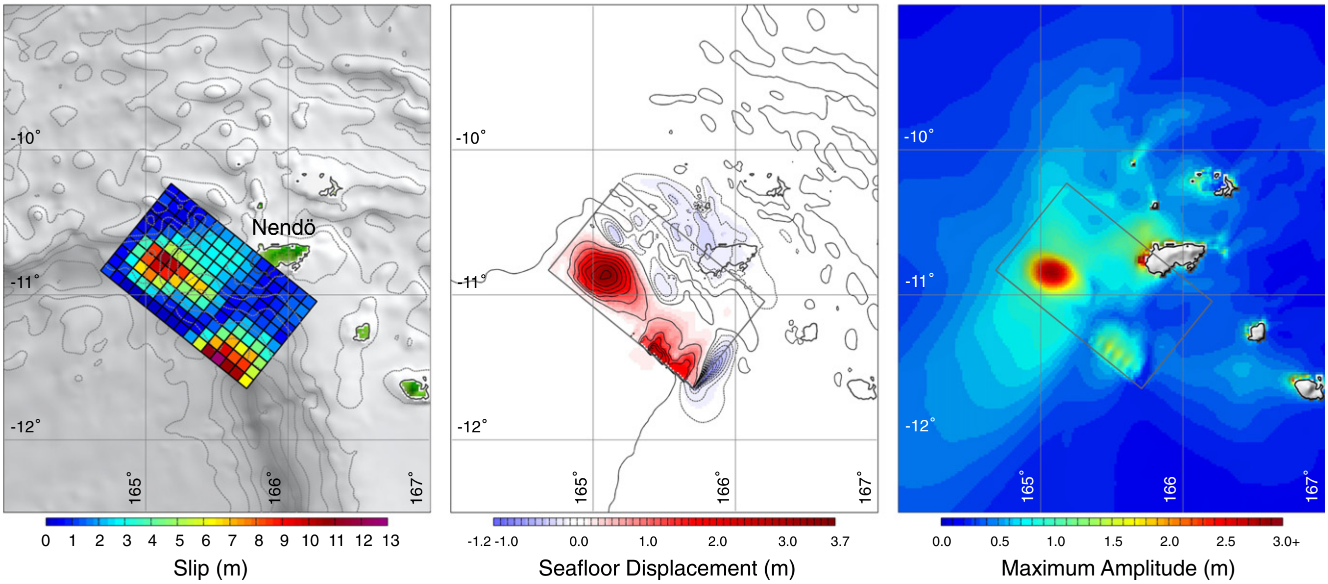

Fig. 8. Maps of the fault slip (left), rock surface vertical displacement (middle), and maximum tsunami wave amplitude (right) for the rupture model for the February 6, 2013 Santa Cruz Islands earthquake obtained by iterative modeling of teleseismic P waves and deep water tsunami recordings from DART buoys. The areas of large slip are near the trench, with the second patch having large slip right to the trench. In the left figure, the dash lines indicate depth contours in 1000 m intervals. In the middle figure, the solid lines indicate the 0.5-m uplift contours, and the dash lines indicate the 0.1-m subsidence contours.

values of 1.5 to 3.4 m from eyewitness. The bathymetry data, however, are not sufficient for runup modeling. The tsunami propagates past the island in 18 min with distinct double crests due to the radial waves from the two slip patches. The two radial waves intersect to form a prominent crest propagating in the southwest direction. These initial tsunami waves are followed by reflected, diffracted, and trapped waves from Nendö.

The southwest Pacific has numerous trenches, seamounts, and shelves that play significant roles in long-wave dynamics. Fig. 10 illustrates the propagation of the tsunami across the ocean to Hawaii.

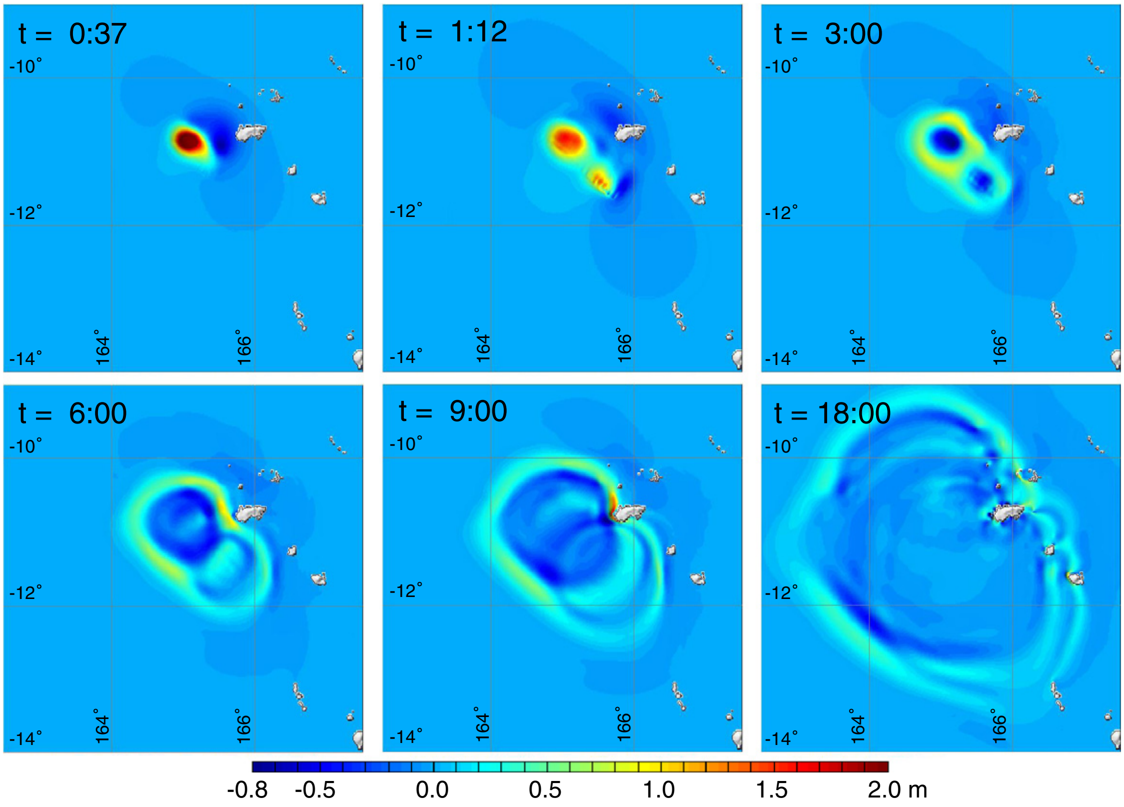

Fig. 9. Snapshots of the computed sea surface elevation showing generation and propagation of the February 6, 2013 Santa Cruz Islands tsunami near the rupture area. The slip patches produce two radial waves that are followed by their reflection and diffraction from Nendö. The two radial waves intersect to produce a dominant crest in the southwest direction. The time scale is in minutes.

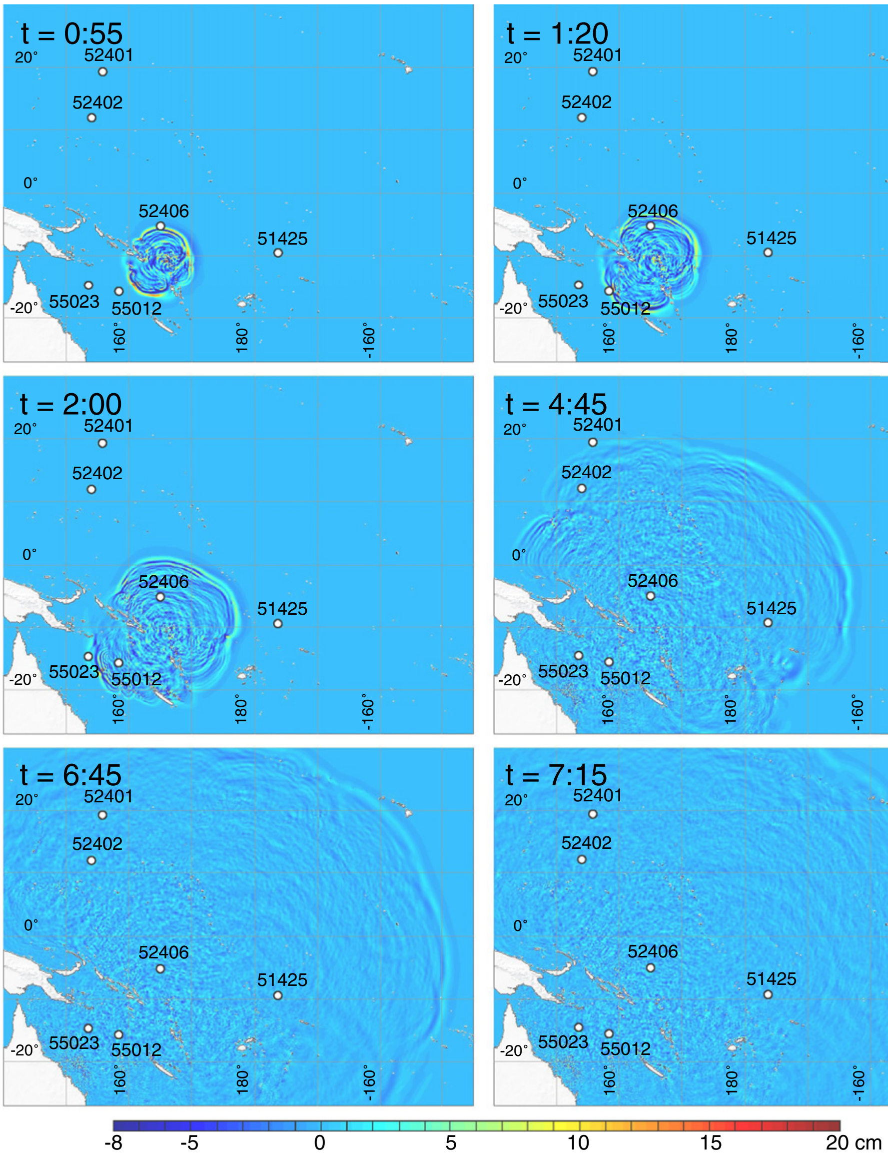

Fig. 10. Snapshots of the computed sea surface elevation showing propagation of the February 6, 2013 Santa Cruz Islands tsunami across the Pacific Ocean. The tsunami maintains two closely-spaced initial waves followed by reflected and diffracted waves from Nendö during the initial hours. White circles indicate DART water level stations. The time scale is h:min.

The larger radial wave from the northwest slip patch reaches DART 52406 in 55 min followed by the smaller radial wave from the southwest slip patch (see supplemental material Animation S2). DART 55012 located directly southwest of the rupture captures the constructive interference of the two radial waves as well as their reflection off Nendö. The waves are attenuated and elongated before reaching DART 55023, which is located slightly off the southwest azimuth in a basin. The tsunami, which reaches DART 52401 in 4 h 45 min after the earthquake, continues to maintain the two closely spaced crests at the front. The two radial waves have merged before arriving at Hawaii around 6 h 45 min. The initial wave crosses the island chain in 30 min with notable attenuation. Meanwhile, the water continues to oscillate in the southwest Pacific due to trapping of tsunami energy by the seamounts and islands. The computed maximum wave amplitude, shown in Fig. 11a, displays strong perturbations of the basic two-lobed azimuthal tsunami radiation pattern expected for a thrust faulting geometry. Intersection of the two radial waves produces a prominent energy beam pointing southwest toward DART 55012. Constructive interference from various wave systems and focusing along island chains result in multiple energy beams across the Pacific. The Gilbert Island chain, which aligns normal to the direction of energy propagation, shelters Hawaii from the tsunami. The computed wave amplitude in Fig. 11b shows a maximum value of 2.5 cm off the insular shelves and a significant reduction across the island chain to 1.6 cm. Standing waves develop over the insular shelves including Penguin Bank, which is known for its role in trapping of tsunami energy and resonance along the island chain (Munger and Cheung, 2008).

Fig. 12 compares the observed and computed waveforms at DART buoys and Hawaii tide gauges. The computed time series have been shifted by up to 5 min to account for delayed arrival to the lack of secondary dispersion effects associated with earth elasticity and water density variation (Tsai et al., 2013). The results show very good agreement in basic waveform, timing, amplitude, and frequency content. At DART 52406 immediately to the north of the source, the model captures the initial wave from the northwest slip patch, slightly overestimates the second wave from the southeast slip patch, and gives good agreement to the reflected and diffracted waves from Nendö. The unique wave pattern and its good agreement with the measurements

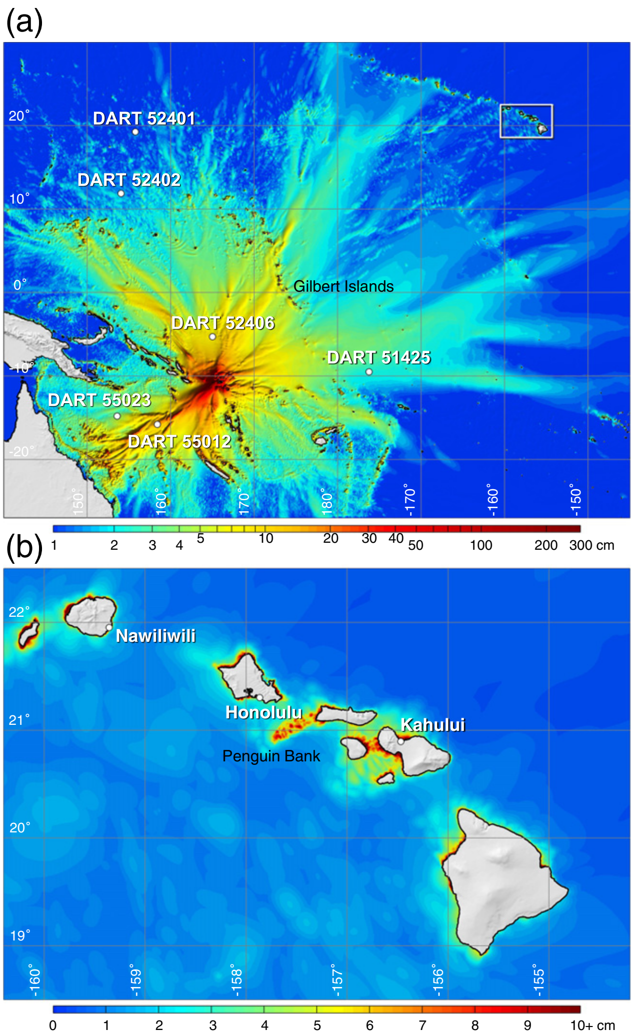

Fig. 11. Maximum wave amplitude of the February 6, 2013 Santa Cruz Islands tsunami across the Pacific and around Hawaii. Constructive interference of wave systems and focusing along island chains results in distinct energy beams across the ocean. The Gilbert Island chain oriented normal to the energy propagation shelters Hawaii from the tsunami. Standing waves develop over the insular shelves of the Hawaiian Islands with notable amplification. White circles indicate water level stations.

are maintained at DART 52402 and 52401 further north. Directly to the southwest on a major energy beam, DART 55012 recorded constructive interference of the two radial waves and their reflections that are followed by weaker diffracted waves from Nendö due to the buoy's reverse azimuth location. Constructive interference of the signals is not evident at DART 55023, which is located off the energy beam. The buoy recorded two closely-spaced initial waves and separate arrivals of the reflections followed by the diffracted waves. DART 51425 due east recorded an initial wave with double peaks. The weaker initial peak likely originated from the smaller and closer southeast slip patch, while the second dominant peak is from the northwest slip patch. The animation of the model results shows merging of the two radial waves before reaching the buoy. The slight overestimations of the first peak at DART 51425 to the east of the source and the second peak at DART 52406, 52402, and 52401 to the northwest support the existence of even more concentrated slip in the southeast of the rupture region. The good agreement at the tide gauge in Honolulu Harbor, which directly opens to the south, indicates accurate depictions of the amounts of slip and the overall fault dimensions. The water around Hawaii behaves as a multimodal resonator that amplifies discrepancies associated with wave period. The overestimation of the subsequent arrivals at Nawiliwili and Kahului on the far side of the respective islands results from slight deviations in the wave periods and *a posteriori* the detailed rupture configurations.

Given the complexity of the tsunami wave pattern in the southwestern Pacific and the resonance behaviors of the water around Hawaii, the match to the recorded data is exceptional. This has motivated the iterative modeling procedures to tune the timing and waveform fits as much as possible by refining the P wave inversion models. Comparison with initial models using deeper (USGS) hypocenters and steeper fault dips (gCMT) in the Supplementary Fig. S1 and S2 highlights the marked improvements achieved for the final model. The modeling of the DART signals provided relatively good constraints on the fault dimensions, trenchward rupture extent, and slip for the rupture model. Our final rupture model is generally compatible with the broadband teleseismic P waves, W-phase observations and very long-period surface waves, R1 STFs, short-period back-projections, and the azimuthally well-distributed DART observations. Despite the spatially localized regions of large seafloor uplift, the model manages to corroborate the near-field wave amplitude reported by eyewitness and reproduce the tsunami waveforms at tide gauges in Hawaii further reassuring its validity.

4. Rupture energy and aftershock sequence

A broadband source spectrum was obtained for the 2013 Santa Cruz Islands earthquake by combining the spectrum of the finite-fault moment rate-function for the preferred model in Fig. 6 for frequencies less than 0.05 Hz with stacks of radiation-pattern- and attenuation-corrected teleseismic broadband P wave spectra for frequencies greater than 0.05 Hz. The source spectrum is compared with a reference ω-squared spectrum for a stress factor of 3 MPa in Fig. 13(a). Estimation of radiated seismic energy from the P wave ground velocity spectra for the frequency band 0.05–1.0 Hz gives a value of 2.15×10^{15} J for the average source velocities indicated in Fig. 13(b). Consideration of the cumulative seismic energy distribution over the full bandwidth from 0.005 to 1.0 Hz indicates that this is about 24% of the total radiated seismic energy, giving a total value of 9.1×10^{15} J. This indicates the importance of accounting for the lower frequency energy for a source with somewhat depleted short-period spectral amplitudes, as found for this event. Using the finite-fault estimate of seismic moment, we obtain a moment-scale radiated energy value of 5.8×10^{-6}, which is in the lower portion of the distribution for interplate earthquake values found by similar procedures, as shown in Fig. 13(c).

The 2013 Santa Cruz Islands event has similar moment-scaled radiated energy to the great 2007 Solomon Islands and 2006 Kurile Islands earthquakes, both of which also ruptured shallow portions of their corresponding megathrusts. The 2013 event appears to essentially be an earthquake doublet, as was the 2007 Solomon Islands event (Furlong et al., 2009). For the 2013 event the two subevents differ in depth on the megathrust, and it is reasonable that the energy release and stress drop on the two patches are not the same, so the overall source spectrum and radiated energy averages the composite effects. Thus, it may be that the second, very shallow subevent which appears to have lower short-period radiation may be similar to a tsunami-earthquake, with very large slip at shallow depth, enhancing the overall tsunamigenesis. This is supported by the short-period $\hat{m}_b$ value of 6.2 (determined following Houston and Kanamori, 1986), which gives $\hat{m}_b$:M_W relative values comparable to those measured for tsunami earthquakes (Fig. 13(d)). As the event appears to be a compound failure, it does not meet an overall characterization as a tsunami earthquake, but it shares with tsunami earthquake attributes of low rupture velocity, large near-trench slip, and somewhat low overall energy and short-period radiation (Lay et al., 2012).

The aftershock sequence is also distinctive in the total absence of larger interplate thrusting aftershocks in the shallow region where

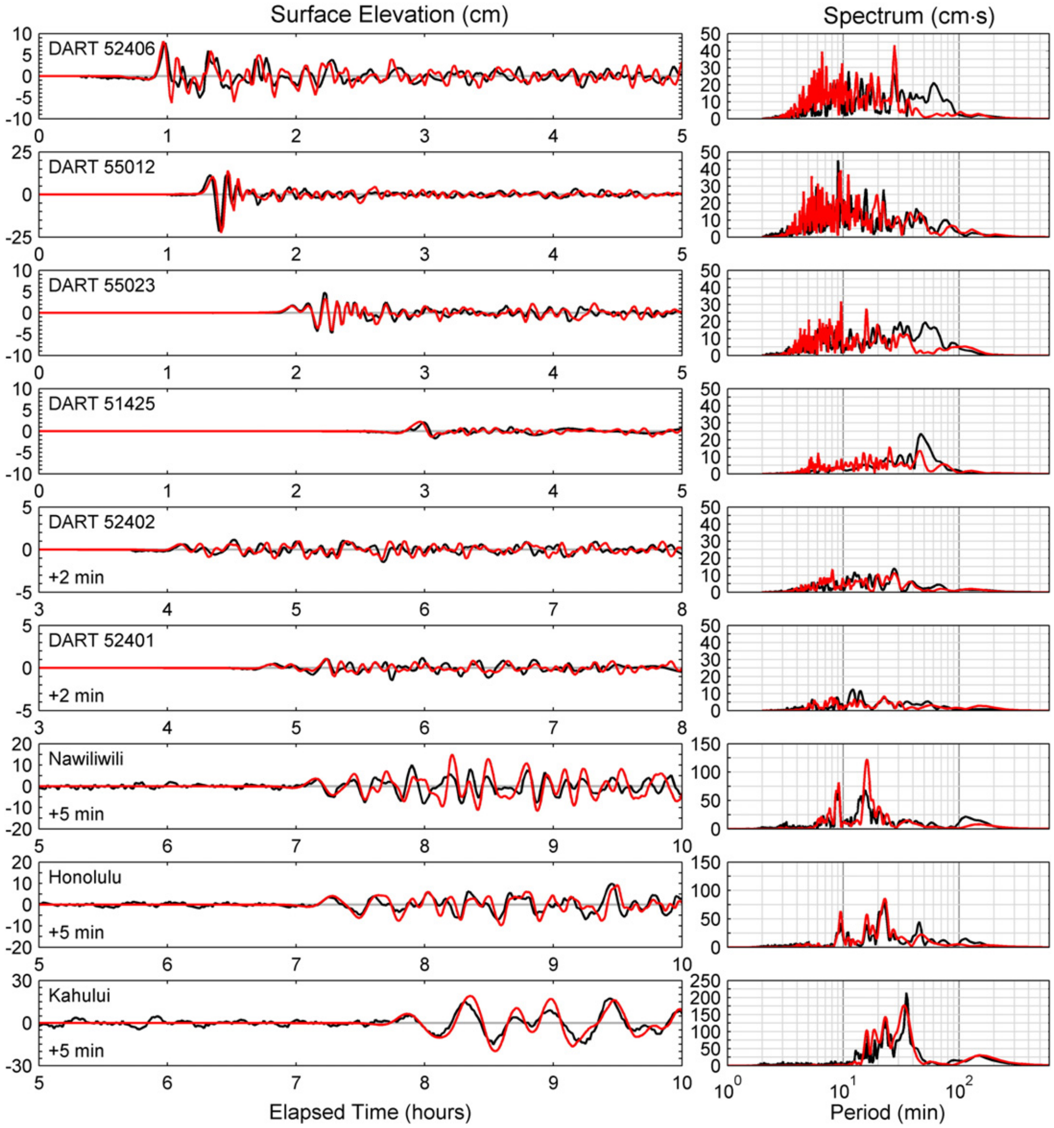

Fig. 12. Comparison of observed (black) and computed (red) sea surface elevation time series (left) and spectra (right) for the February 6, 2013 Santa Cruz Islands tsunami. Shifting of the computed time series is necessary to match the arrival time and indicated as appropriate. The positions of the DART buoys and tide gauges relative to the source and the pattern of peak tsunami amplitudes are shown in Fig. 11.

large coseismic slip occurred (Fig. 1b). This is further depicted in Fig. 14, which shows a time-line for the full sequence, with available M_w values and gCMT best double-couple focal mechanisms being shown (for events with $M_w \geq 5.2$) or m_b values from the USGS if no gCMT solution is available. There are only 3 thrust events among the aftershocks with mechanism determinations, and all of these are likely intraplate, although the most recent event could be on the deeper megathrust (it has relatively large source depth and steep dip). The largest events have been upper plate strike-slip or outer rise normal faulting events. This lack of large interplate thrust events in the aftershock series contrasts with the foreshock sequence in the southern part of the mainshock rupture zone near the trench that had five moderate-size thrust events. One possibility is that the two large-slip patches resulted in near total stress drop on the megathrust even while the stress changes induced on adjacent intraplate fault systems proved very seismogenic. The total sequence has 164 events with $m_b \geq 5.0$, 55 having $m_b \geq 5.5$, 19 having $M_w \geq 6.0$, and 4 having $M_w \geq 7.0$, including the mainshock. The cumulative moment of the aftershock sequence is about 20% of the mainshock moment. The diverse aftershock faulting appears to be associated with the complex plate distortions near the bend in the plate boundary and the generally high productivity observed for seismicity in this region. It is clear that the overall aftershock zone is much larger than the coseismic slip zone, as observed for the 1966 and 1980 events to the south, and caution should be exercised in inferring rupture expansion velocity or rupture area since none of the larger events are actually on the megathrust fault that ruptured in the mainshock.

5. Conclusion

The 2013 Santa Cruz Islands earthquake ruptured the northernmost portion of the Vanuatu trench where the plate boundary curves strongly westward and extends to the Solomon Islands Trench. The earthquake has M_w estimates of 8.0 to 8.1, making it the largest seismologically well-quantified event in the region, and it struck an area where no prior large event had been located since at least 1900. The earthquake has a shallow-dipping thrust-faulting solution indicating that it ruptured on the plate boundary. It produced substantial

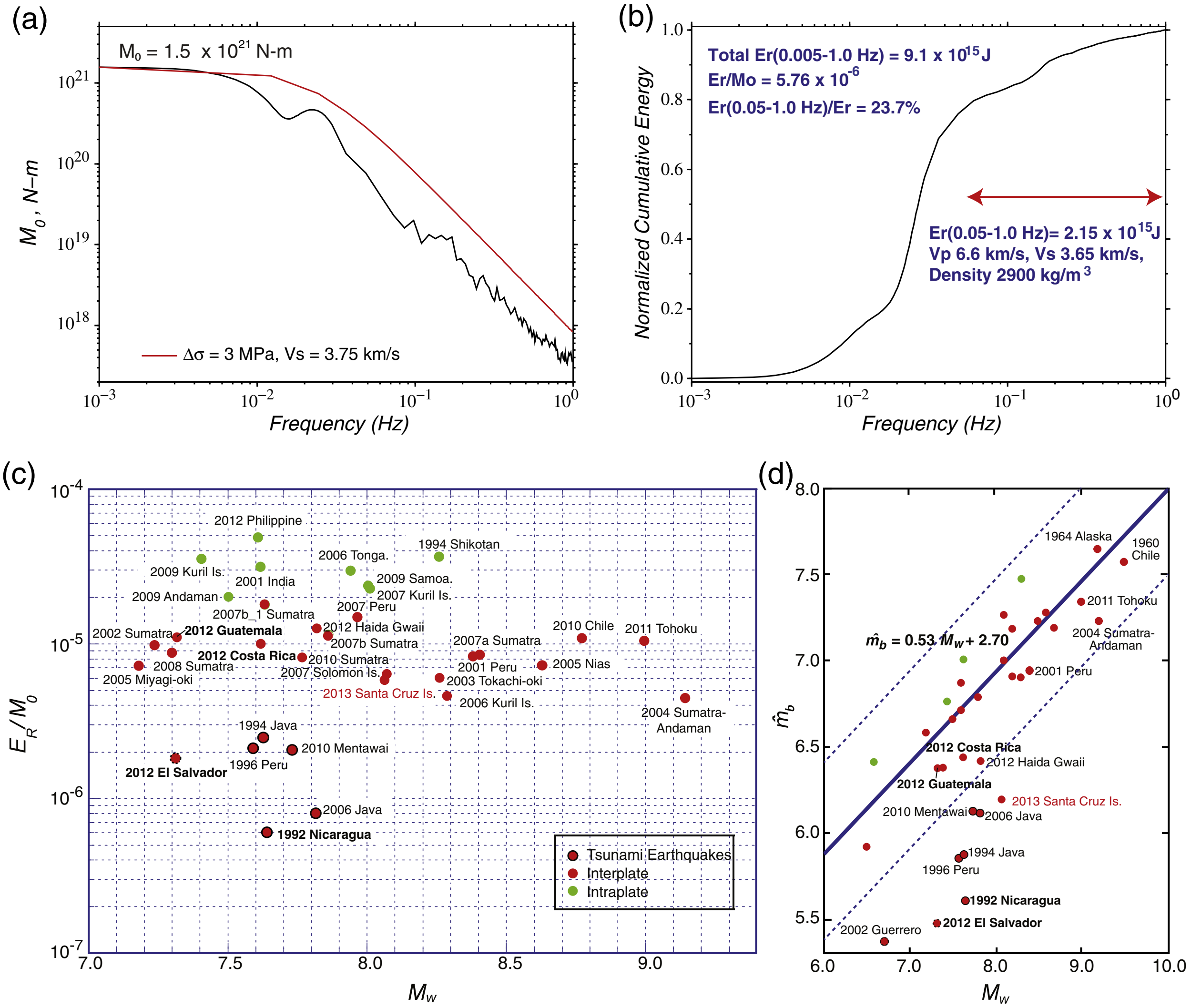

Fig. 13. (a) Source spectrum for the February 6, 2013 Santa Cruz Islands (M_w 8.0) earthquake obtained from combining the spectrum of the finite-source model from P wave inversion (Fig. 6) for frequencies below 0.05 Hz with an averaged spectra of broadband P waves for frequencies from 0.05 to 1.0 Hz. A reference ω-squared source spectrum with a stress drop parameter of 3 MPa is shown for comparison. (b) Cumulative energy as a function of frequency over the passband from 0.005 to 1.0 Hz. The radiated energy from the 0.05 to 1.0 Hz passband is 2.15 × 10^{15} J, and the total energy over the 0.005–1.0 Hz passband, Er, is 9.1 × 10^{15} J. The ratio of Er/M_0 = 5.76 × 10^{-6}. (c) Er/M_0 values for large interplate and intraplate earthquake are plotted as a function of M_w, including the value for the 2013 Santa Cruz Islands earthquake (highlighted with red labeling). (d) Short-period $\widehat{m}_b$ measurements for large earthquakes, with the measured value for the 2013 Santa Cruz Islands earthquake highlighted with red labeling. The event had low short-period P wave amplitudes consistent with a tsunami earthquake, but the moment scaled total energy ratio is typical of interplate ruptures on the shallow megathrust like the 2007 Solomon Islands and 2006 Kuril Islands events as shown in (c).

tsunami on nearby islands and at deep-water DART buoy sensors, indicating significant seafloor uplift. Using constraints on the faulting geometry provided by long-period seismic waves and short-period P wave back-projections, a finite-fault solution is obtained by iterative modeling of broadband P-waves and DART tsunami recordings. A satisfactory fit is obtained to all data sets for a rupture with two large-slip patches, with a southeastward rupture progression. The second patch locates very close to the trench, and appears to have lower seismic moment than the first patch, large slip and low short-period seismic radiation. The event is thus a compound doublet rupture that is not an end-member tsunami earthquake event although it shares some common attributes with such earthquakes in other regions. There are no large aftershocks known to have interplate thrusting solutions among a vigorous sequence with strike-slip, normal-faulting and compressional-faulting events that spread over a broad region. The large-slip patches do not overlap the large-slip region of previous large events located to the southeast. The lack of interplate thrusting aftershock activity may indicate near total stress-drop on the rupture zone even while intense aftershock activity on other faults occurred.

Supplementary data to this article can be found online at http://dx.doi.org/10.1016/j.tecto.2013.07.001.

Acknowledgments

This work made use of GMT, SAC and Matlab software. The IRIS DMS data center was used to access the seismic data from Global Seismic Network and Federation of Digital Seismic Network stations. We thank an anonymous reviewer for constructive comments. DART buoy data were obtained from the NOAA National Data Buoy Center. This work was supported by NSF grants EAR-1245717 (T. L.).

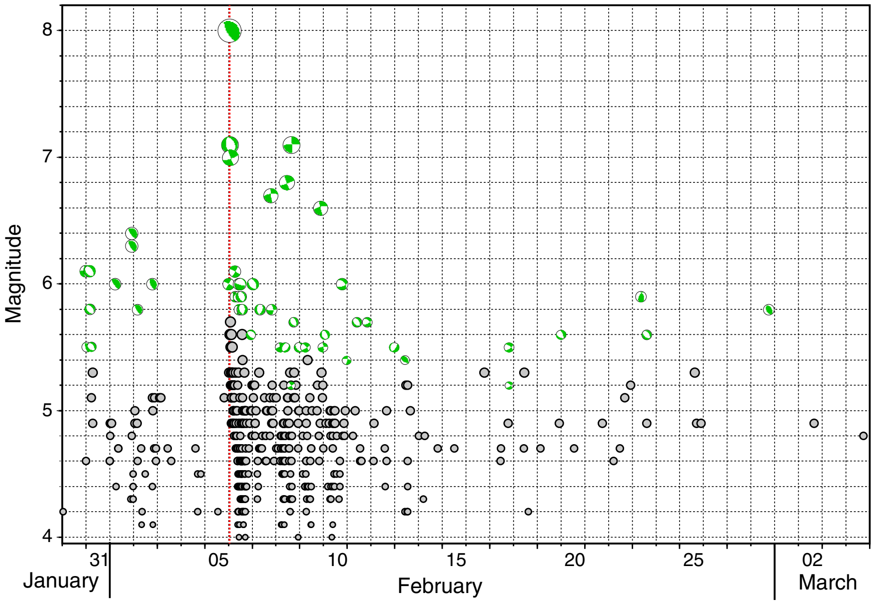

Fig. 14. The 2013 Santa Cruz Island earthquake sequence timeline, with the gCMT focal mechanism for the larger events being included. The sequence initiated with normal faulting and strike-slip faulting in the upper plate, then after a day became an interplate thrust sequence, and a few days later the mainshock thrust occurred, initiating an intense aftershock sequence with the larger events being strike-slip and normal faulting. There have only been three compressional aftershocks, and only one of these is plausibly on the megathrust, and that is at relatively large depth.

References

Allen, T.I., Marano, K., Earle, P.S., Wald, D.J., 2009. PAGER-CAT: a composite earthquake catalog for calibrating global fatality models. Seismological Research Letters 80 (1), 50–56.

Ammon, C.J., Kanamori, H., Lay, T., 2008. A great earthquake doublet and seismic stress transfer cycle in the central Kuril islands. Nature 451, 561–566.

Bassin, C., Laske, G., Masters, G., 2000. The current limits of resolution for surface wave tomography in North America. Eos, Transactions of the American Geophysical Union 81, F897.

Cleveland, K.M., Ammon, C.J., Lay, T., 2013. Large earthquake processes in the northern Vanuatu subduction zone. Journal of Geophysical Research (in preparation).

Felzer, K.R., Abercrombie, R.E., Ekström, G., 2004. A common origin for aftershocks, foreshocks, and multiplets. Bulletin of the Seismological Society of America 94 (1), 88–98.

Furlong, K., Lay, T., Ammon, C.J., 2009. A great earthquake rupture across a rapidly evolving three-plate boundary. Science 324, 226–229.

Houston, H., Kanamori, H., 1986. Source spectra of great earthquakes: teleseismic constraints on rupture process and strong motion. Bulletin of the Seismological Society of America 76, 19–42.

Kanamori, H., Rivera, L., 2008. Source inversion of W-phase: speeding up seismic tsunami warning. Geophysical Journal International 175, 222–238.

Kaverina, A., Dreger, D., Antolik, M., 1998. Source process of the 21 April, 1997 Santa Cruz Island earthquake (M_w 7.8). Geophysical Research Letters 26 (21), 4027–4030.

Kikuchi, M., Kanamori, H., 1991. Inversion of complex body waves III. Bulletin of the Seismological Society of America 81, 2335–2350.

Lay, T., Kanamori, H., 1980. Earthquake doublets in the Solomon Islands. Physics of the Earth and Planetary Interiors 21 (4), 283–304.

Lay, T., Kanamori, H., Ammon, C.J., Hutko, A.R., Furlong, K., Rivera, L., 2009. The 2006–2007 Kuril Islands great earthquake sequence. Journal of Geophysical Research 114, B11308. http://dx.doi.org/10.1029/2008JB006280.

Lay, T., Ammon, C.J., Kanamori, H., Rivera, L., Koper, K.D., Hutko, A.R., 2010. The 2009 Samoa–Tonga great earthquake triggered doublet. Nature 466 (7309), 964–968.

Lay, T., Yamazaki, Y., Ammon, C.J., Cheung, K.F., Kanamori, H., 2011. The great 2011 Tohoku-oki (M_w 9.0) earthquake: comparison of deep-water tsunami signals with finite-fault rupture model predictions. Earth, Planets and Space 63 (7), 797–801.

Lay, T., Kanamori, H., Ammon, C.J., Koper, K.D., Hutko, A.R., Ye, L., Yue, H., Rushing, T.M., 2012. Depth-varying rupture properties of subduction zone megathrust faults. Journal of Geophysical Research 117, B04311. http://dx.doi.org/10.1029/2011JB009133.

McCann, W.R., Nishenko, S.P., Sykes, L.R., Krause, J., 1979. Seismic gaps and plate tectonics: seismic potential for major boundaries. Pure and Applied Geophysics 117, 1082–1147.

Munger, S., Cheung, K.F., 2008. Resonance in Hawaii waters from the 2006 Kuril Islands tsunami. Geophysical Research Letters 35 (7), L07605. http://dx.doi.org/10.1029/2007GL032843.

Nishenko, S.P., 1991. Circum-Pacific seismic potential: 1989–1999. PAGEOPH 135, 169–259.

Okada, Y., 1985. Surface deformation due to shear and tensile faults in a half space. Bulletin of the Seismological Society of America 75 (4), 1135–1154.

Pacheco, J.F., Sykes, L.R., 1992. Seismic moment catalog of large shallow earthquakes, 1900 to 1989. Bulletin of the Seismological Society of America 82, 1306–1349.

Ruff, L.J., 1996. Large earthquakes in subduction zones: segment interaction and recurrent times. In: Bebout, G.E., Scholl, D.W., Kirby, S.H., Platt, J.P. (Eds.), Subduction: Top to Bottom. AGU Geophysical Monograph, vol. 96, pp. 91–104.

Schwartz, S., Lay, T., Ruff, L., 1989. Source process of the great 1971 Solomon Islands doublet. Physics of the Earth and Planetary Interiors 56, 294–310.

Tajima, F., Kanamori, H., 1985a. Aftershock area expansion and mechanical heterogeneity of fault zones within subduction zones. Geophysical Research Letters 12, 345–348.

Tajima, F., Kanamori, H., 1985b. Global survey of aftershock area expansion patterns. Physics of the Earth and Planetary Interiors 40, 77–134.

Tajima, F., Ruff, L.J., Kanamori, H., Zhang, J., Mogi, K., 1990. Earthquake source processes and subduction regime in the Santa Cruz Islands region. Physics of the Earth and Planetary Interiors 61, 269–290.

Tanioka, Y., Satake, K., 1996. Tsunami generation by horizontal displacement of ocean bottom. Geophysical Research Letters 23, 861–864.

Trabant, C., Hutko, A.R., Bahavar, M., Karstens, R., Ahern, T., Aster, R., 2012. Data products at the IRIS DMC: stepping-stones for research and other application. Seismological Research Letters 83 (6), 846–854. http://dx.doi.org/10.1785/0220120032.

Tsai, V.C., Ampuero, J.-P., Kanamori, H., Stevenson, D.J., 2013. Estimating the effects of earth elasticity and variable water density on tsunami speeds. Geophysical Research Letters 40, 492–496. http://dx.doi.org/10.1002/GRL.50147.

Xu, Z., Schwartz, S.Y., 1993. Large earthquake doublets and fault plane heterogeneity in the northern Solomon Islands subduction zone. Pure and Applied Geophysics 140, 365–390.

Xu, Y., Koper, K.D., Sufri, O., Zhu, L., Hutko, A.R., 2009. Rupture imaging of the M_w 7.9 12 May 2008 Wenchuan earthquake from back projection of teleseismic P waves. Geochemistry, Geophysics, Geosystems 10, Q04006. http://dx.doi.org/10.1029/2008GC002335.

Yamazaki, Y., Kowalik, Z., Cheung, K.F., 2009. Depth-integrated, non-hydrostatic model for wave breaking and run-up. International Journal for Numerical Methods in Fluids 61 (5), 473–497.

Yamazaki, Y., Cheung, K.F., Kowalik, Z., 2011a. Depth-integrated, non-hydrostatic model with grid nesting for tsunami generation, propagation, and run-up. International Journal for Numerical Methods in Fluids 67 (12), 2081–2107.

Yamazaki, Y., Lay, T., Cheung, K.F., Yue, H., Kanamori, H., 2011b. Modeling near-field tsunami observations to improve finite-fault slip models for the 11 March 2011 Tohoku earthquake. Geophysical Research Letters L00G15. http://dx.doi.org/10.1029/2011GL049130.